EUROPEAN ORGANIZATION FOR NUCLEAR RESEARCH

August 29, 2025

Measurement of three-body ppp correlation functions in Pb-Pb collisions with ALICE Run 3

Austėja Jurgaitytė[1]
Supervisors: Laura Šerkšnytė[2], Maximiliano Puccio[2]

1. Vilnius University
2. CERN

Email: austeja.jurgaityte23@gmail.com

Abstract

The interactions of Λ hyperons with nucleons are of high interest for the studies of the composition of the inner core of neutron stars, where the appearance of strangeness might be energetically favourable [9]. A precise knowledge of the two- and three-body interactions at small distances is required to define the equation of state at such high densities, but they are not yet well constrained by the existing experimental data. It was recently proven that we can study the strong interaction in three-hadron systems by measuring femtoscopic correlation functions of particles emitted with distances of around 1 fm in high-energy pp collisions at the LHC [5]. Another interesting test-bed for the calculations is Pb-Pb collisions, where the source size is much larger and thus allows to test already available theory in a different system. This note presents the measurement of ppp correlation in Pb-Pb collisions, at $\sqrt{s} = 5.36$ TeV energy using Run 3 2023 data.

Introduction

Theoretical models describing the properties of nuclei and hypernuclei indicate that three-body forces are necessary to satisfactorily describe available measurements. These forces become especially significant at high densities as those reached in the inner cores of neutron stars, where they can even exceed several times the nuclear saturation density. As this density increases, the chemical potential of nucleons might reach values at which it is more energetically favourable to introduce new degrees of freedom, such as hyperons, despite their larger masses [9].

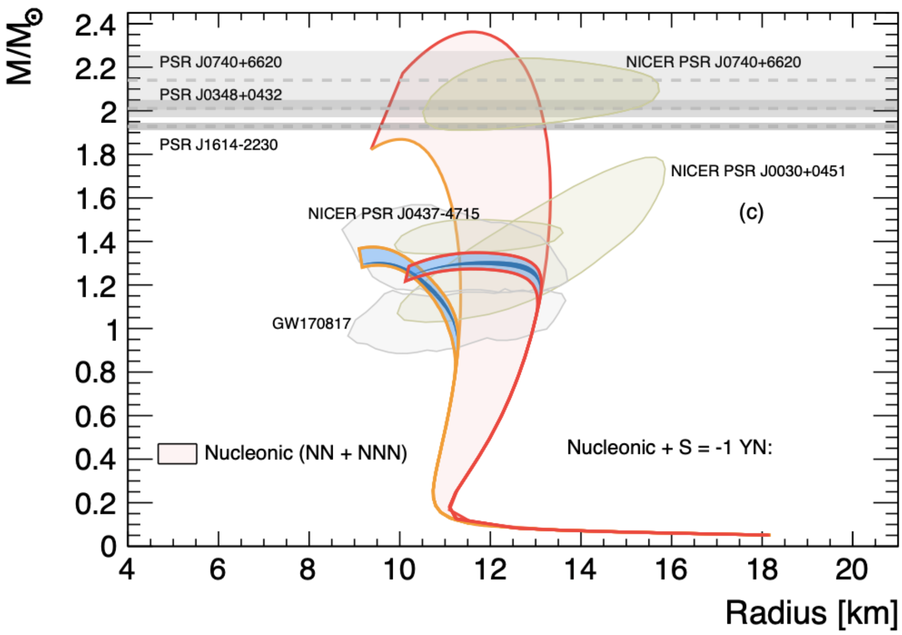

Fig. 1: Mass - radius relation for neutron stars. The grey horizontal bands and green shaded areas represent astrophysical measurements, the bands show theoretical predictions. Red - orange band takes only NN and NNN interactions into account, while red and blue ones introduce YN interactions [9].

Fig. 1 showcases the mass - radius relations for neutron stars, which are obtained for specific equations of state via the Tolman–Oppenheimer–Volkoff (TOV) equations. The EoS calculations are strongly dependent on the interactions between particles that are considered. The grey horizontal bands and green shaded areas represent astrophysical measurements, meanwhile red and blue bands show theoretical predictions. However, when hyperon-nucleon (YN) interactions (represented by blue bands) are included into the calculations, the equations of state can no longer explain the observed heavy neutron stars, due to the hyperon appearance softening the equation of state. This is known as the hyperon puzzle [9]. One of the prime candidates to solve it is the repulsive YNN interactions, but currently they are not well constrained experimentally. Three-body femtoscopic ppp and ppΛ correlation measurements are a novel way to access strong interaction in ppp and ppΛ systems and study this phenomenon [5, 7].

Correlation function

In femtoscopy, the usual observable is two-particle momentum correlation function (Eq. 2), which is defined as a ratio of the probability of finding a particle pair at certain relative momenta and a product of the corresponding single particle probabilities at those relative momenta (Eq. 1) [5, 8].

$$C(\mathbf{p}_1, \mathbf{p}_2) \equiv \frac{P(\mathbf{p}_1, \mathbf{p}_2)}{P(\mathbf{p}_1)P(\mathbf{p}_2)}. \tag{1}$$

During high-energy collisions numerous other particles are produced. If one would take two of these produced particles, for a very short moment in time right after the collision, these two particles might be close enough in phase-space to experience final state interaction. This interaction changes their momenta in their center of mass frame - leading to momentum-space correlations between them [8]. We can measure this change as the so-called femtoscopic correlation function:

$$C(k^*) = N\frac{N_{same}(k^*)}{N_{mixed}(k^*)} = S(r^*)|\Psi(k^*,r^*)|^2 d^3r^*. \tag{2}$$

The right side of this equation is the Koonin-Pratt equation to calculate the correlation function, where $S(r^*)$ is the distribution of the relative distances of particle pairs in the pair rest frame (denoted by the $*$) — the so-called source function. The wave function of the particle pair relative motion is denoted by $\psi(\mathbf{r}^*,\mathbf{k}^*)$ where $\mathbf{k}^* = (\mathbf{p}_1^* - \mathbf{p}_2^*)/2$ is the relative momentum in pair rest frame. The wave function encapsulates the details of the particle interaction and drives the shape of the correlation function [8].

The left side of Eq. 2 is the experimental two-particle correlation function. N_{SE} and N_{ME} represent distributions of pairs of particles as a function of their relative momenta in pair rest frame. N_{SE} particle pairs are taken from the same collision, while the mixed event distribution N_{ME} is formed by taking two particles from two different collisions [8].

Three-body correlation functions can be constructed analogously, as written in Eq. 3:

$$C(Q_3) = N\frac{N_{same}(Q_3)}{N_{mixed}(Q_3)} = \int \rho^5 d\rho d\Omega_\rho S(\rho,\rho_0)|\Psi(\rho,Q_3)|^2. \tag{3}$$

Here Q_3 is the Lorenz-invariant three-particle hypermomentum, as defined in Eq. 4, ρ is the hyperradius, Ω_ρ corresponds to the set of five hyperangles, and $|\Psi(\rho,Q_3)|^2$ is the square of the scattering wave function for the three particles.

$$Q_3 = \sqrt{-q_{ij}^2 - q_{jk}^2 - q_{ki}^2} \tag{4}$$

Recently, a mathematical framework was developed to calculate the three-body correlations functions theoretically following the right side of Eq. 3. It is done employing hyperspherical harmonic approach and details on theory can be found in ref. [5, 6].

ALICE detector

The data used in this analysis was collected using the A Large Ion Collider Experiment detector, otherwise known as ALICE, designed to study Pb-Pb collisions at LHC (pictured in Fig. 2.) It is a 16 m high complex apparatus, comprised of many individual detector systems. For this analysis, the most relevant of these layers are the Inner Tracker System (ITS), Time Projection Chamber (TPC) and Time-of-Flight (TOF) detectors. The ITS is the innermost detector, using Monolithic Active Pixel Sensors (MAPS) technology for charged particle identification and track reconstruction. It has seven layers, three of which are in the Inner Barrel (IB). The Time Projection Chamber is cylindrical, gas-filled detector with a central high-voltage electrode and read-out chambers at each end. It's purpose is tracking and particle identification. As charged particles pass through, they ionise the gas and then those free electrons drift towards the read-out chambers. By measuring the drift time, energy loss and location of the collected charge in the TPC, one can then reconstruct a particle's trajectory and also identify it. The Time-of-Flight layer is located outside the TPC. Using Multigap Resistive Plate Chambers (MRPCs), it helps identify charged particles with high momentum by measuring their flight time from the collision point to the detector [3, 4].

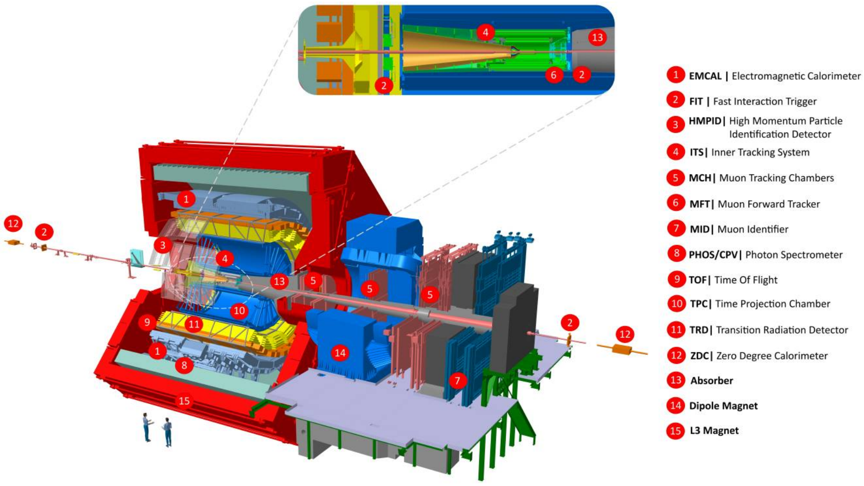

Fig. 2: The ALICE detector in its Run 3 configuration [4].

Selection criteria

Throughout the duration of this project, we have analyzed PbPb collisions at $\sqrt{(s)} = 5.36$ TeV from 8 different data-taking periods (all collected in 2023, see Table 1), totalling to roughly 0.8 Pb of data. Neural networks were used to identify the particles during the data skimming. To save resources, some of the checks regarding track selection were performed using only a subset of the data (specified next to each check).

Table 1: The different data-taking periods used in the final correlation function analysis and their data sizes.

Dataset name	Size (TB)
zzn	68.8
zzg	18.6
zzf	8
zzk_medium	99.7
zzo_medium	91
zzl	166.3
zzi	89.3
zzm	245.2
Combined	786.9

The event selection criteria include filtering out events with a Z-component of the primary vertex position, that is further than 10 cm away from the centre of the detector. The $sel8$ selection is also applied, rejecting physically uninteresting events such as beam gas collisions. Additionally, only events that contain at least one proton particle fulfilling the loosest systematic selection criteria are used.

The selection criteria used to identify proton candidates are described in Table 2, while below it is described how these selection criteria were chosen and why they are different compared to equivalent ALICE analysis of three body correlations in pp collisions.

Table 2: Selection criteria used for the data to obtain the final correlation functions.

Selection criterion	Value
Pseudorapidity	$\lvert\eta\rvert < 0.8$
Transverse momentum	$0.8 < p_t < 2$ GeV/c
ITS hits	$n_{ITS} = 7$
TPC cluster	$nTPC > 90$
Crossed TPC rows	$n_{crossed} > 80$
TPC min crossed rows/findable clusters	$n_{crossedRows} > 0.83$
Distance of closest approach xy	$\lvert DCA_{xy}\rvert < 0.1$ cm
Distance of closest approach z	$\lvert DCA_z\rvert < 0.2$ cm
Particle identification	$n_{\sigma,comb} < 3$

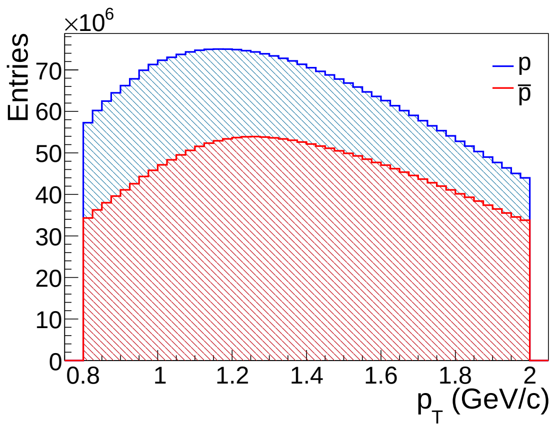

Fig. 3: Combined particle and antiparticle distributions from all data-taking periods used.

Most of these selection criteria were taken from the Run 3 three-body ppp femtoscopy data analysis in pp collisions [2], exceptions being the transverse momentum p_t constrains and the requirements for observed particle "hits" in the ITS, used for track reconstruction. This is due to the fact that the data contamination has a notable contamination in particles with low transverse momentum p_t, which was observed due to disagreement between particle and antiparticle correlation functions. Figure 4 compares ppp and $\bar{p}\bar{p}\bar{p}$ correlation functions in different centrality bins, using two different minimum transverse momentum p_t selection criteria – 0.5 GeV/c on the left side and 0.8 GeV/c on the right. As seen in figure 4, the correlation functions for particles and antiparticles are severely different while the physics involved are expected to be the same. The correlation function is expected to be rather flat at low Q3 values based on theoretical predictions. Thus the antiproton correlation function can be expected to be more correct than proton one, also due to the peak observed in particle correlation function at $Q_3 = 1.8$ GeV/c. From comparison between different centrality ranges shown in Figure 4, it is also visible that the largest effect of contamination is in the case of high centralities, becoming less pronounced in lower centralities. Here the zzm_medium dataset (subset of zzm, 96.7 TB) is used, the other selection criteria applied are as described in 2.

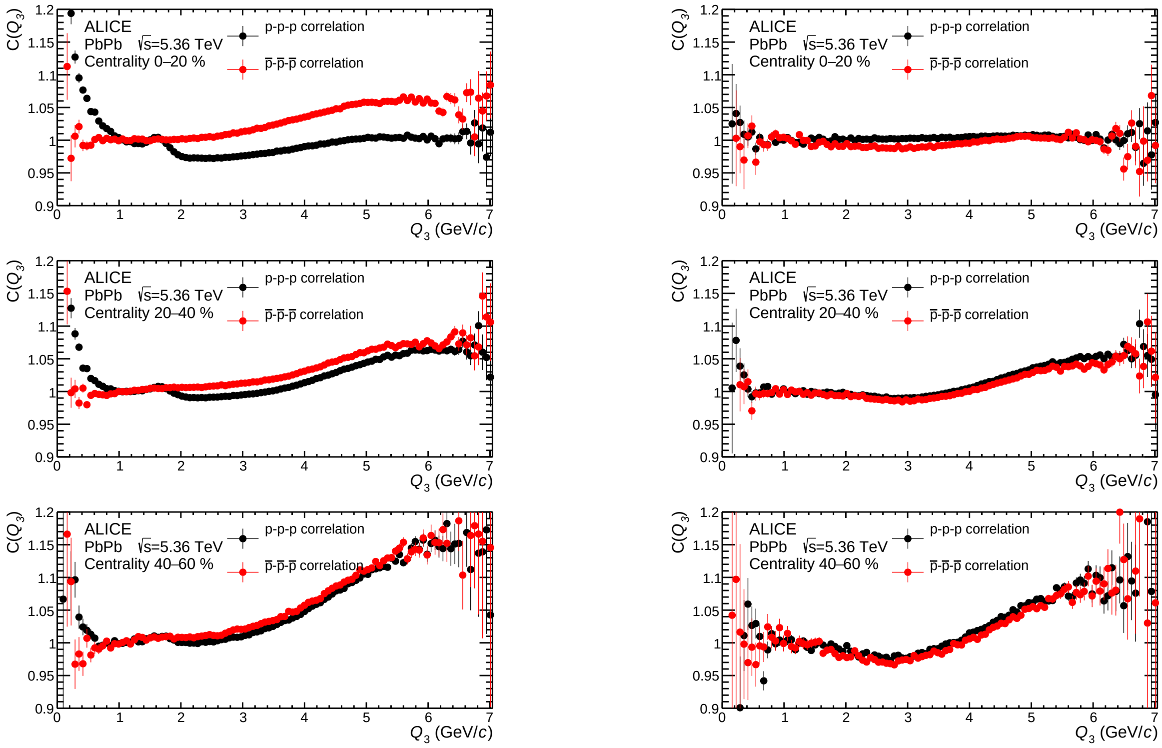

Fig. 4: p-p-p and $\bar{p}$-$\bar{p}$-$\bar{p}$ correlation function comparison for different centrality ranges, using two different minimum transverse momentum p_t selection criteria – 0.5 GeV/c on the left side and 0.8 GeV/c on the right.

Numerous tests were done trying out different selection criteria to filter out the contamination and allowing us to use the less harsh p_t minimum selection criterion, thus reclaiming more data.

One way we tried to fix it was by using a different selection criterion for the track reconstruction in ALICE Inner Tracking System – ITS. In figure 5 we can see in how many ITS layers (left histogram describing the total, while IB layers only are seen on the right) the particle clusters used for track reconstruction were observed for the data from the zzm_medium data sample.

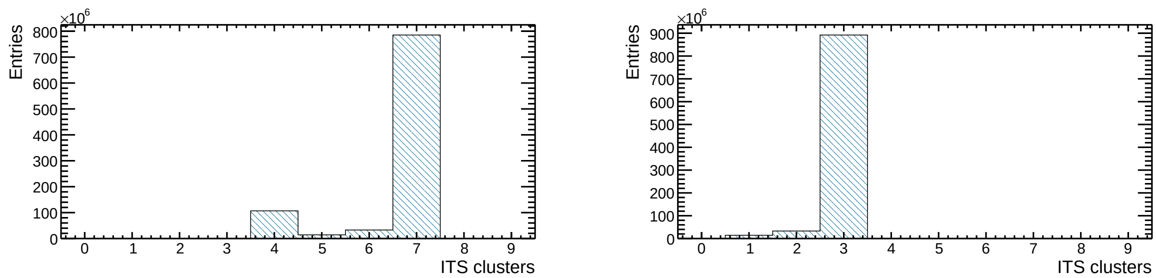

Fig. 5: Distribution of number of ITS layers with hits used for track reconstruction. The histogram on the left shows the total number of ITS layers, while the right shows only the inner barrel (IB) layers.

In the initial analysis we use selection criteria requiring at least one hit in the inner barrel which was sufficient in the previous pp analysis to remain with mainly tracks that have 7 total hits in the ITS. However, for PbPb analysis this results in a substantial amount tracks having only 4 total hits, as shown in Figure 5. Thus we tested a selection criteria requiring total 7 hits. The logic behind this would be that particles that come from the primary collision should pass through all seven layers, thus this could reduce contamination from weak decays and secondary particles from material interactions. The correlation functions obtained using the $n_{ITS} = 7$ selection criterion are shown in figure 6 on the left panel, while correlation functions obtained with $n_{ITSIB} >= 1$ are on the right. As seen in Fig. 6, the improvement introduced by the requirement of 7 ITS hits results in particle and antiparticle correlation functions that are more similar to each other, so this selection criterion was kept in future analysis.

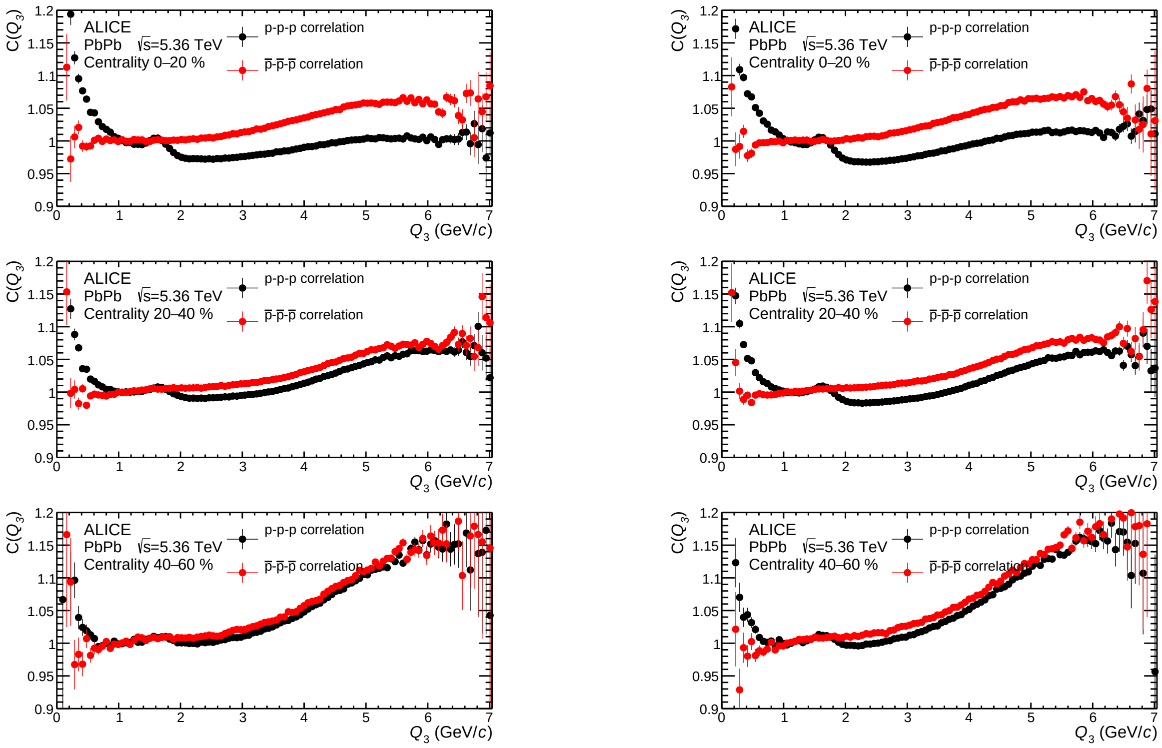

Fig. 6: p-p-p and $\bar{p}$-$\bar{p}$-$\bar{p}$ correlation function comparison for different centrality ranges, using two different requirement criteria for observed particle "hit" in the ITS – $n_{ITS} = 7$ on the left side and $n_{ITSIB} >= 1$ on the right.

Next, using a DCA selection criterion with p_t dependence was considered. In the code the maximum allowed DCA_{xy} to vertex dependence function was changed from $0.0105 + 0.035/pT^{1.1}$ to $abs(dcaxy) < 0.004 + 0.013/pT$. The resulting correlation functions for the zzm_medium dataset are seen in figure 7. The minimum requirement for the transverse momentum P_t here is 0.8 GeV/c. There was no significant improvement observed.

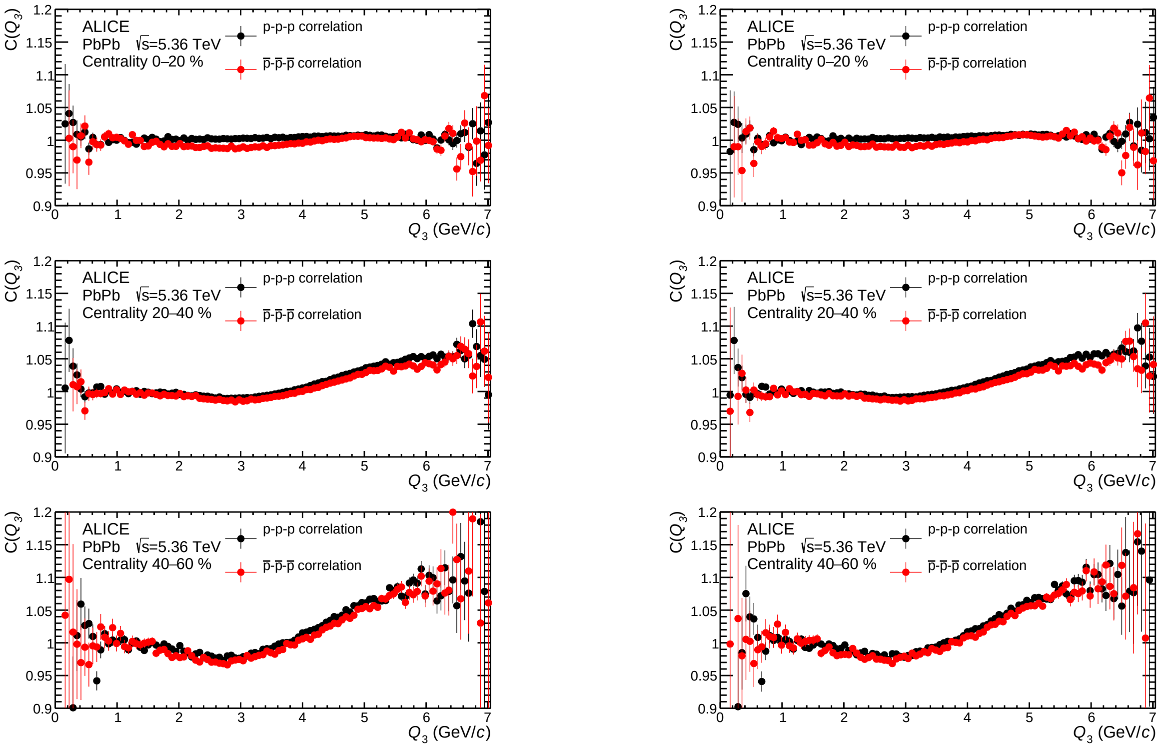

Fig. 7: p-p-p and $\bar{p}$-$\bar{p}$-$\bar{p}$ correlation function comparison for different centrality ranges, using two different DCA selection criteria – one that is strictly less than 0.1 cm in the X and Y axes and 0.2 cm in the Z axis(left panel) and a p_T dependent cut as described in the main text (right). Minimum transverse momentum requirement p_t is 0.8 GeV/c.

The difference in using the DCA p_t dependant selection requirement was also compared using minimum transverse momentum P_t requirement of 0.5 GeV/c, in case low momentum tracks were more affected (figure 8). Only slight differences were observed and only for the case, where minimum p_T is 0.5 GeV/c. As in final analysis the minimum pt was kept 0.8 GeV/c, where no significant differences are observed for the different DCA requirements, we chose to not use this selection criteria further for this analysis.

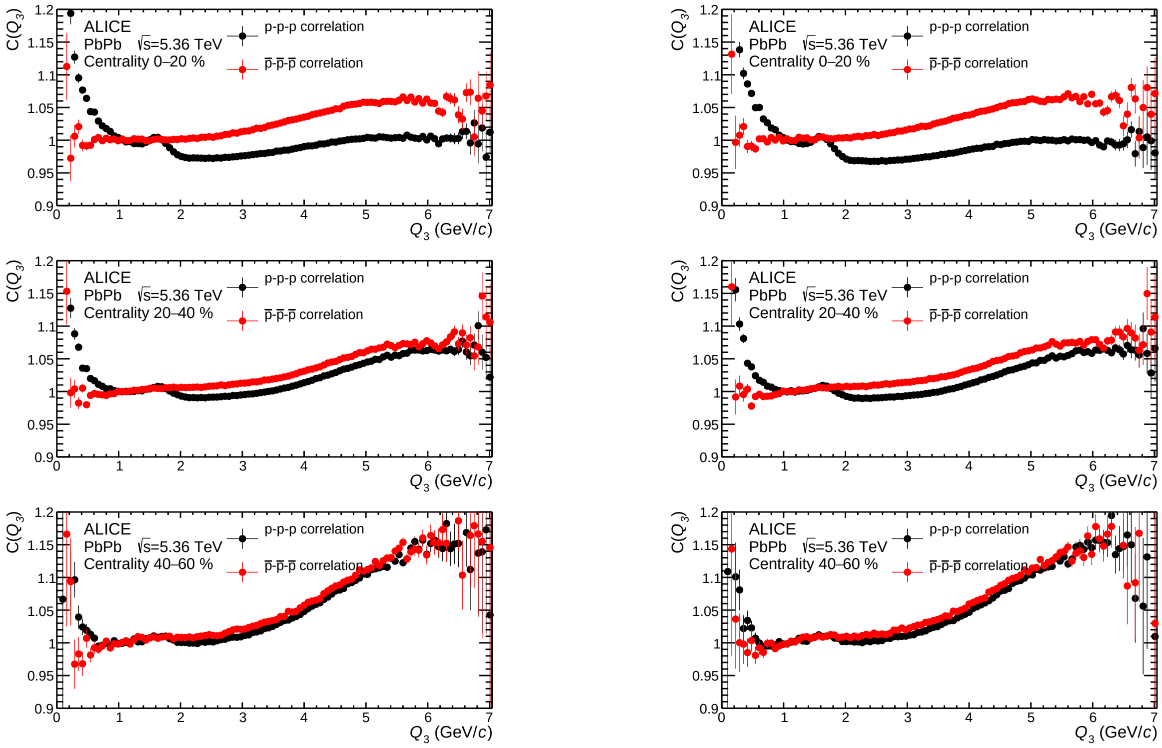

Fig. 8: p-p-p and $\bar{p}$-$\bar{p}$-$\bar{p}$ correlation function comparison for different centrality ranges, using two different DCA selection criteria – one without p_t dependence on the left and the p_t dependant selection criterion on the right. Minimum transverse momentum requirement is p_t is 0.5 GeV/c.

Next, neural networks were used to identify particles in order to try and reduce contamination (minimum transverse momentum requirement of $p_t = 0.8$ GeV/c in Fig. 9 and minimum transverse momentum requirement of $p_t = 0.5$ GeV/c in Fig. 10, zzm_medium dataset.). The results showed less of a difference between particle and antiparticle correlation functions in the higher centrality region at low Q_3. This, coupled with the fact that this method of particle determination is used in other Pb-Pb analyses, lead to the decision of using neural networks for PID's in this analysis.

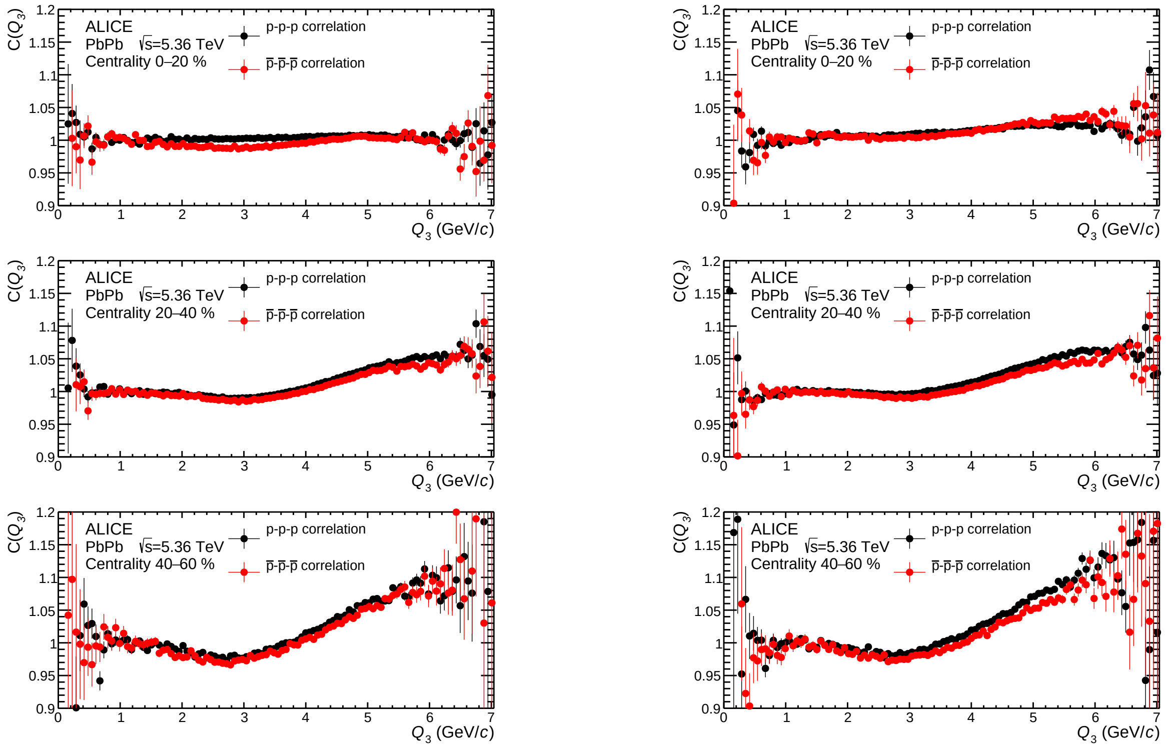

Fig. 9: p-p-p and $\bar{p}$-$\bar{p}$-$\bar{p}$ correlation function comparison for different centrality ranges, using two PID determination methods - one without neural networks (left) and one using them (right)(minimum transverse momentum requirement is $p_t = 0.8$ GeV/c).

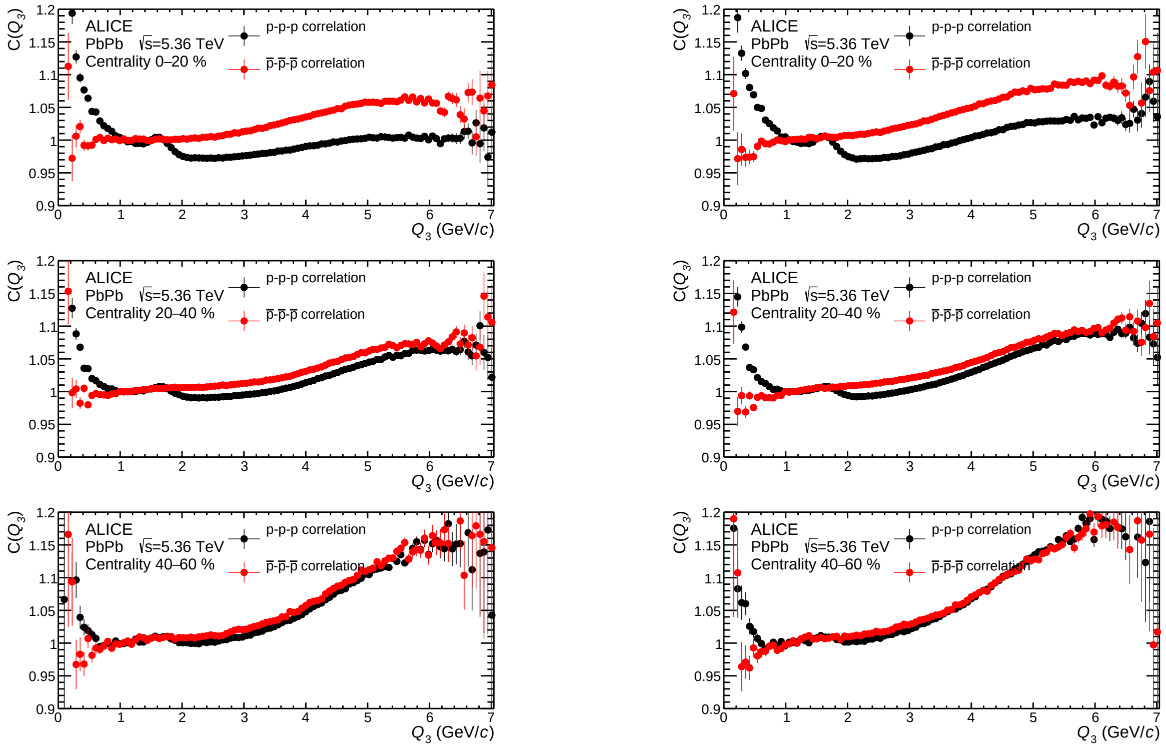

Fig. 10: p-p-p and $\bar{p}$-$\bar{p}$-$\bar{p}$ correlation function comparison for different centrality ranges, using two PID determination methods - one without neural networks (left) and one using them (right)(minimum transverse momentum requirement is $p_t = 0.5$ GeV/c).

In another test, represented in Fig. 11 it was noticed that there is a substantial amount of low p_t tracks that have a number of shared clusters almost equal to the total clusters (visible especially in the left panel, as a diagonal yellow line at the upper part of the distribution.) That is why we decided to try using a different selection criterion for number of allowed shared TPC clusters, decreasing them from 160 to 70 – this would help to remove duplicate particle tracks. The test was done both with minimum transverse momentum p_t requirements of $p_t = 0.5$ GeV/c (see Fig. 12) and $p_t = 0.8$ GeV/c (as seen in Fig. 13). Both of the figures show the old criteria of maximum 160 shared TPC clusters on the left panel and the new criteria of 70 on the right. However, the improvement in correlation function shapes was minimal. This new analysis criterion was tested out on the zzo_medium dataset and was not kept in the final analysis.

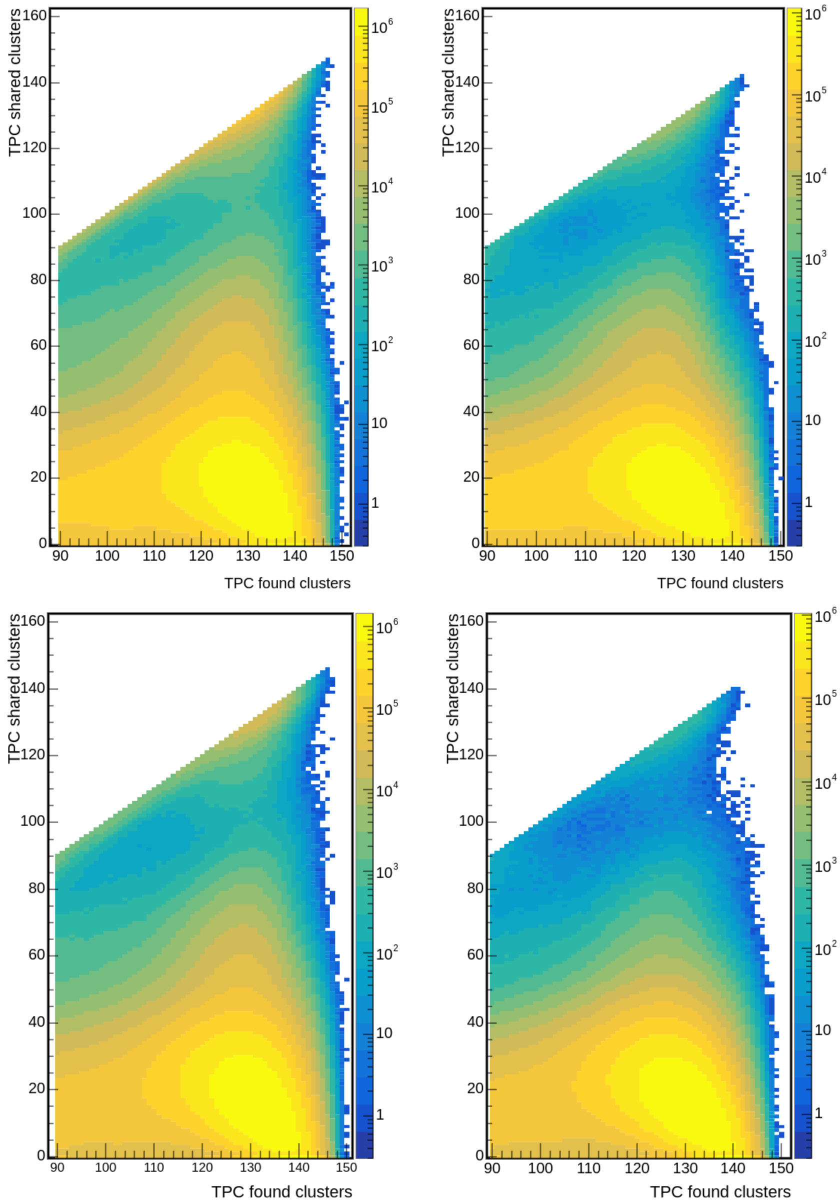

Fig. 11: Shared vs found TPC clusters, which were used for track reconstruction. The left panel represents using the minimum $p_t = 0.5$ GeV/c requirement for particles, while $p_t = 0.8$ GeV/c is on the right. The top panel is for particles, while the bottom is for antiparticles. Obtained from data in the zzm dataset.

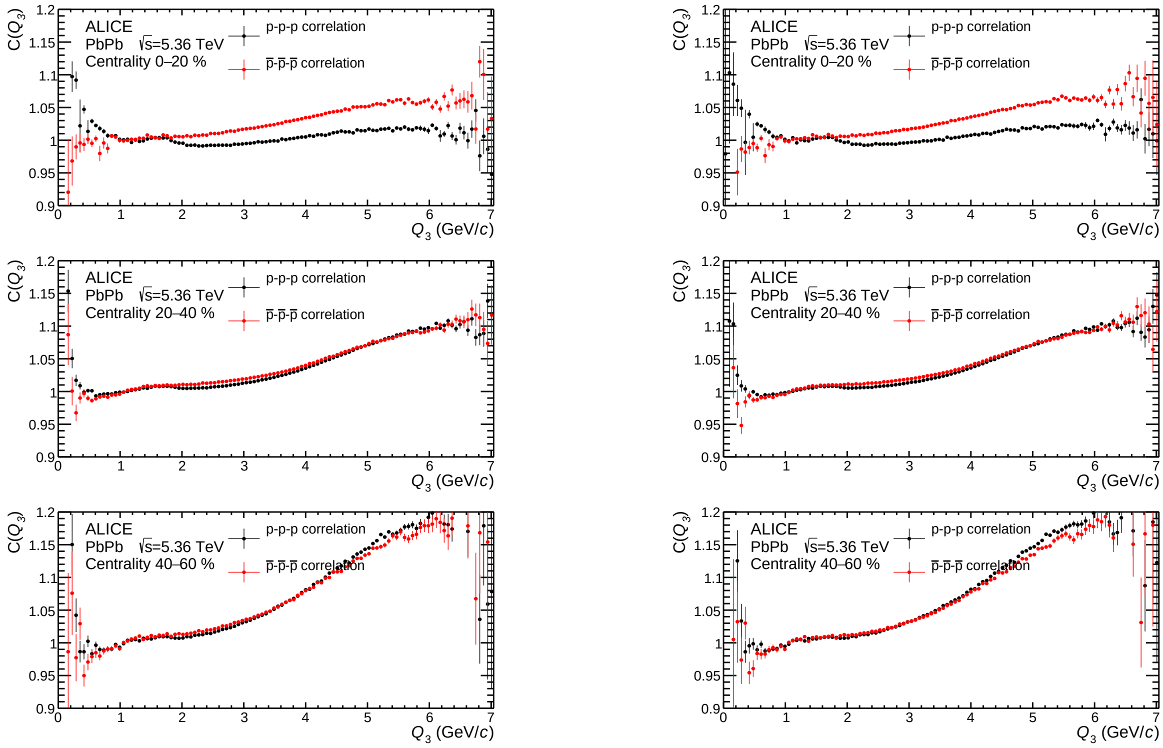

Fig. 12: p-p-p and $\bar{p}$-$\bar{p}$-$\bar{p}$ correlation function comparison for different centrality ranges, using two different shared TPC cluster selection criteria – 160 shared clusters allowed on the left side correlation functions and 70 on the right correlation functions, $p_t = 0.5$ GeV/c.

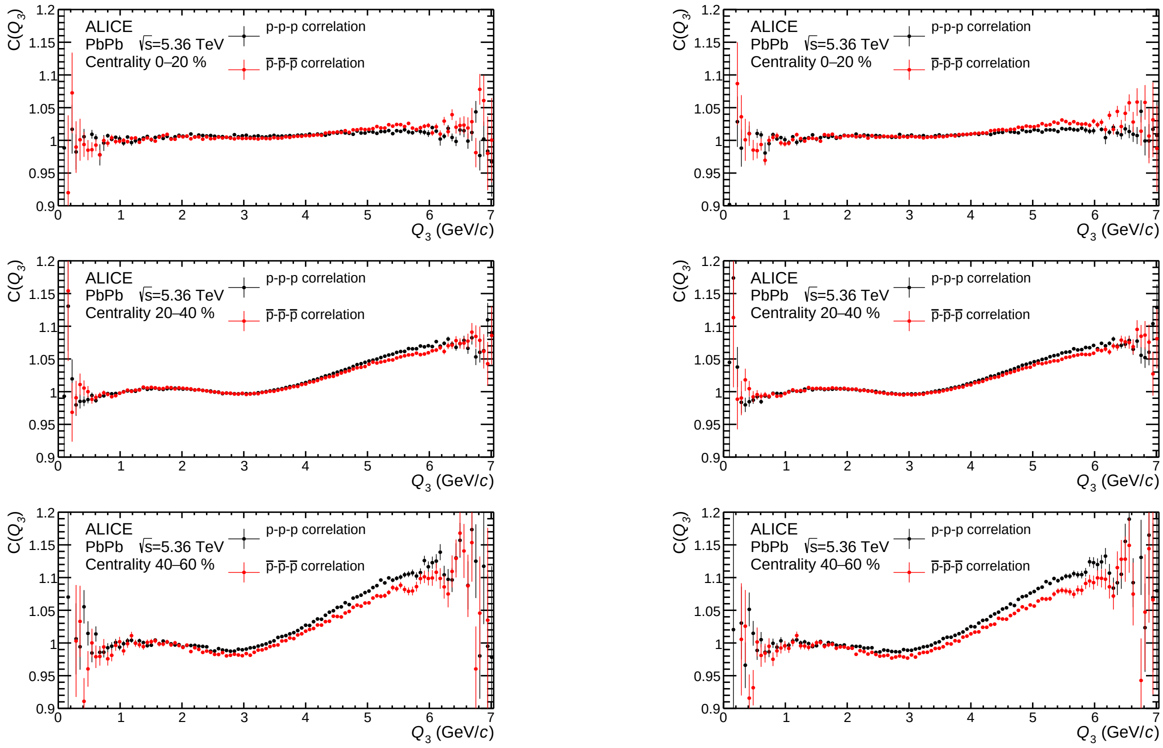

Fig. 13: p-p-p and $\bar{p}$-$\bar{p}$-$\bar{p}$ correlation function comparison for different centrality ranges, using two different shared TPC cluster selection criteria – 160 shared clusters allowed on the left side correlation functions and 70 on the right correlation functions, $p_t = 0.8$ GeV/c.

A stricter $n\sigma_{comb}$ (quantifies how many standard deviations a particle's measured properties deviate from what is expected for a proton) criterion was also tried out on the zzm_medium dataset (minimum p_t = 0.5 GeV/c), as seen in Fig. 14. It was changed from $n\sigma_{comb} = 3$ (left panel) to $n\sigma_{comb} = 2$ (right). This was done in hopes of reducing contamination from particle misidentification, however, there was no noticeable improvement.

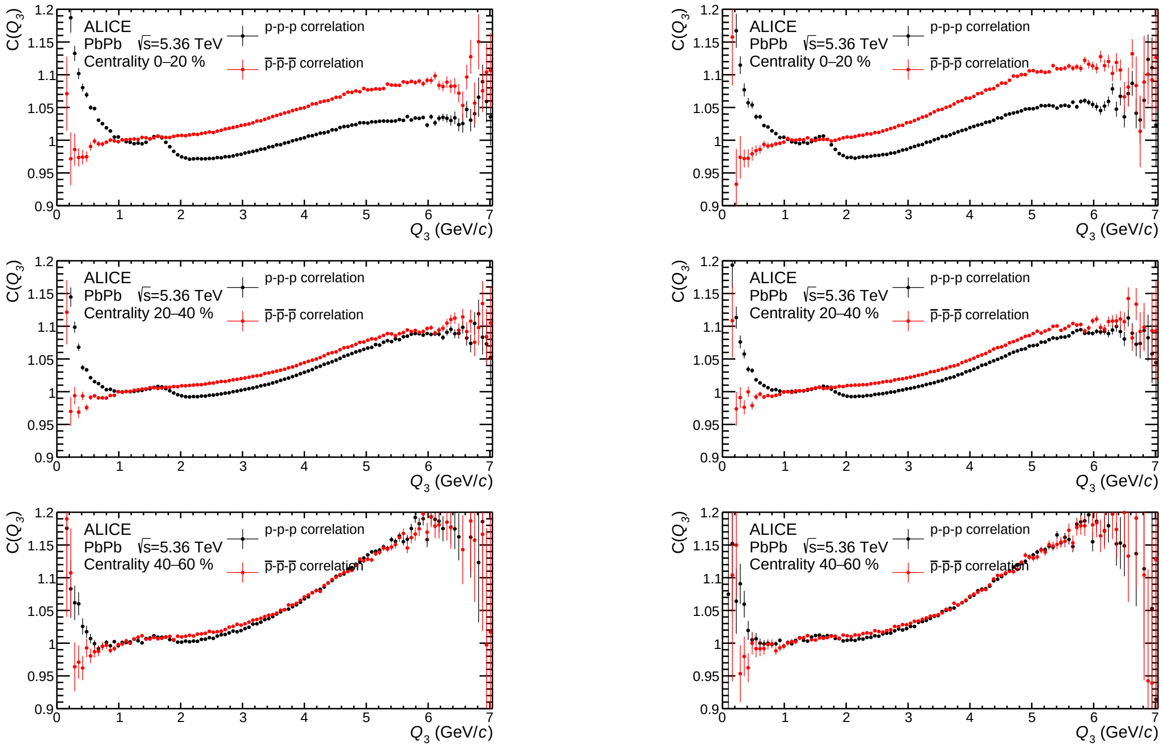

Fig. 14: p-p-p and $\bar{p}$-$\bar{p}$-$\bar{p}$ correlation function comparison for different centrality ranges, using $n\sigma_{comb} = 3$ requirement on the left panel and $n\sigma_{comb} = 2$ on the right. The requirement for transverse momentum p_t was a minimum of 0.5 GeV/c)

Different normalisation was also tried out to see how well the correlation function shapes agree at high Q3. All previously shown correlation functions were normalised between 1.0 and 1.2 GeV/c, but in Fig. 15 normalisation is between 4.0 and 5.0 GeV/c as it was noticed that the particle and antiparticle correlation functions were running parallel in this region. However, for main results we use the standard 1 to 1.2 GeV/c normalization, where the correlation functions seem to be flat.

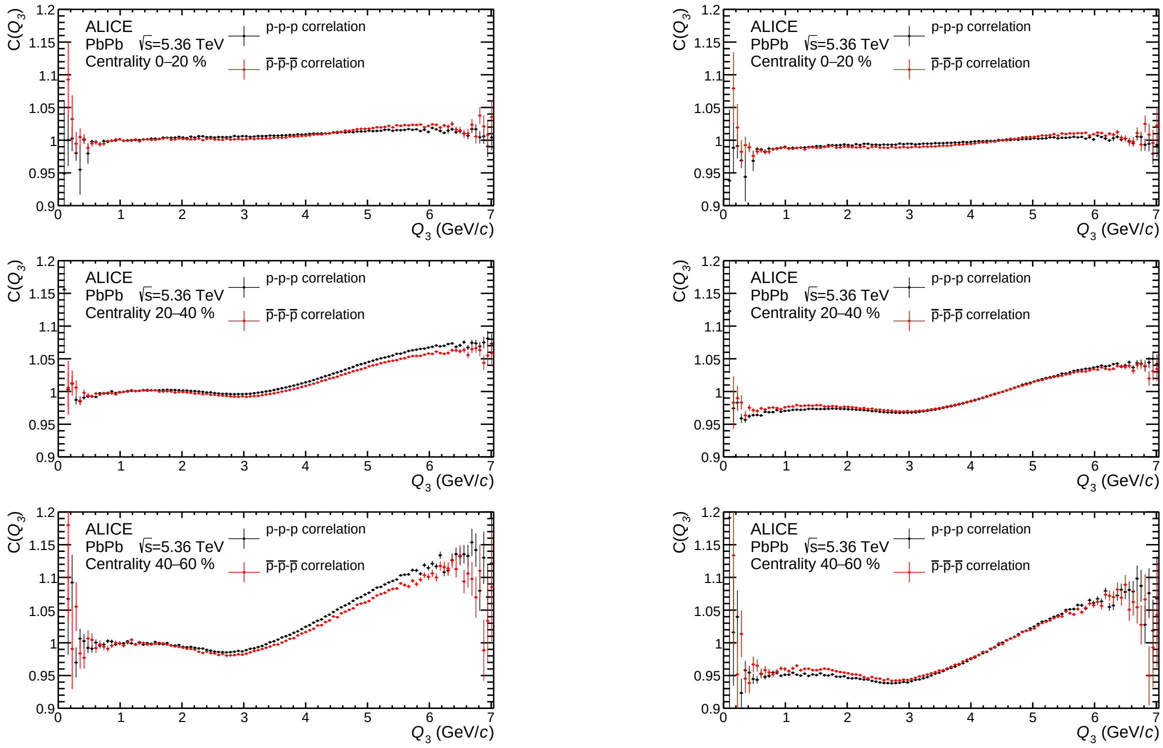

Fig. 15: p-p-p and $\bar{p}$-$\bar{p}$-$\bar{p}$ correlation function comparison for different centrality ranges, using two different normalisation intervals – between 1.0 and 1.2 GeV/c on the left side and 0.8 GeV/c on the right.

In summary, using a DCA selection criterion with p_t dependence and the stricter limitation of maximum shared TPC clusters (70 instead of 160) had no effect on the contamination seen in particles, thus were discarded in the rest of the analysis. A stricter $n\sigma_{comb}$ requirement of 2 instead of 3 also did not solve the contamination problem. The helping criteria changes were requiring all 7 ITS hits, using a stricter minimum transverse momentum cut of 0.5 GeV/c and using neural networks for particle identification; these requirements were implemented when obtaining the final results.

Particle purity

In order to understand the reliability of the obtained results, particle purity must be determined. Particle purity tells us, which fraction of our particles are actual protons and antiprotons. We evaluate the purity by performing fits of the combined $n\sigma$ in TOF and TPC distributions for different p_T ranges. This could also be done employing MC simulations, however, the MC in Run 3 is still undergoing improvements [2].

The combined TPC and TOF $n\sigma_{comb} = \sqrt{n\sigma_{TPC}^2 + n\sigma_{TOF}^2}$ was obtained as a function of p_T to obtain purity as a function of p_T. The projections are taken to have the $n\sigma_{comb}$ distribution for specific p_t bins which are then fitted by the sum of the signal function described in Eq. 5. and background function described in Eq. 6 [2].

$$f(x) = [0] \cdot x \cdot exp(\frac{-x^2 + [1]^2}{2[2]^2} \cdot I_0(\frac{x \cdot [1]}{[2]^2}) \tag{5}$$

$$f(x) = [3] + [4] \cdot x + [5] \cdot exp(-[6] \cdot x) + [7] \cdot exp(-0.5 \cdot (\frac{x - [8]}{[9]})^2) \tag{6}$$

First, the signal function 5 is pre-fitted onto the data in the 0 - 2.5 $n\sigma_{comb}$ range when p_t is in [0.8, 0.98) GeV/c and 0 - 3 $n\sigma_{comb}$ range when the p_t is in [0.98, 2] GeV/c. The background function Eq. 6 is also pre-fitted in the $n\sigma_{comb}$ range from 4 to 9. The parameters obtained from these fits are then used as starting parameters in the full function fit, which is the sum of signal and background, giving us the final parameters for the total function (see Fig. 17 - 18.)

Then, the purity is obtained by integrating the signal and the full fit function between 0 and 3 $n\sigma_{comb}$ and calculating the ratio signal/total, as seen in Fig. 16. This is done for three datasets (zzm_medium, zzi and zzo_medium) to confirm that the purity does not differ much between the datasets used. In the future, improvement to the fits should be made to smooth out the fits and obtain more accurate purities, especially in the p_T ranges where the resulting purities suddenly change by 10%.

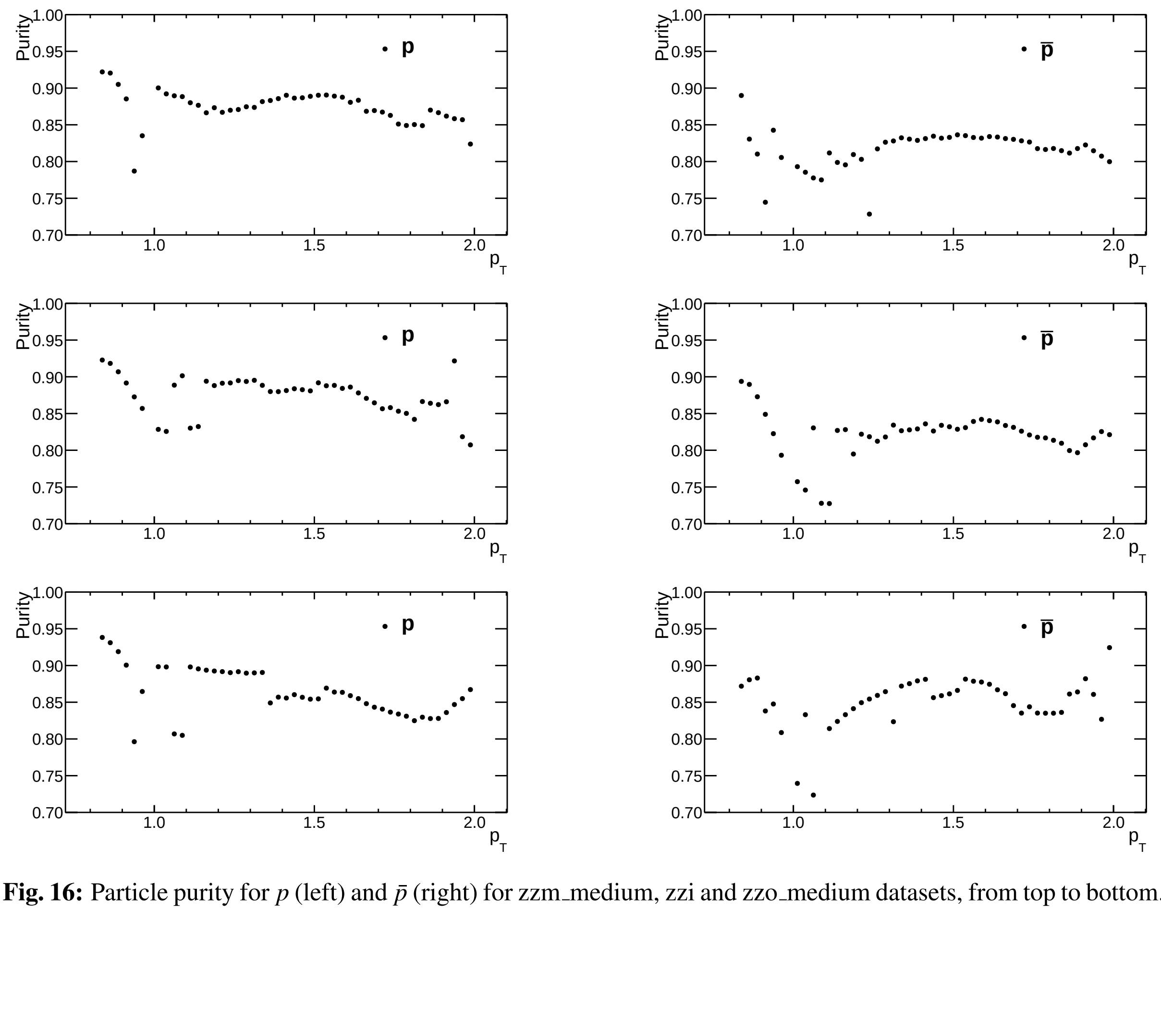

Fig. 16: Particle purity for p (left) and $\bar{p}$ (right) for zzm_medium, zzi and zzo_medium datasets, from top to bottom.

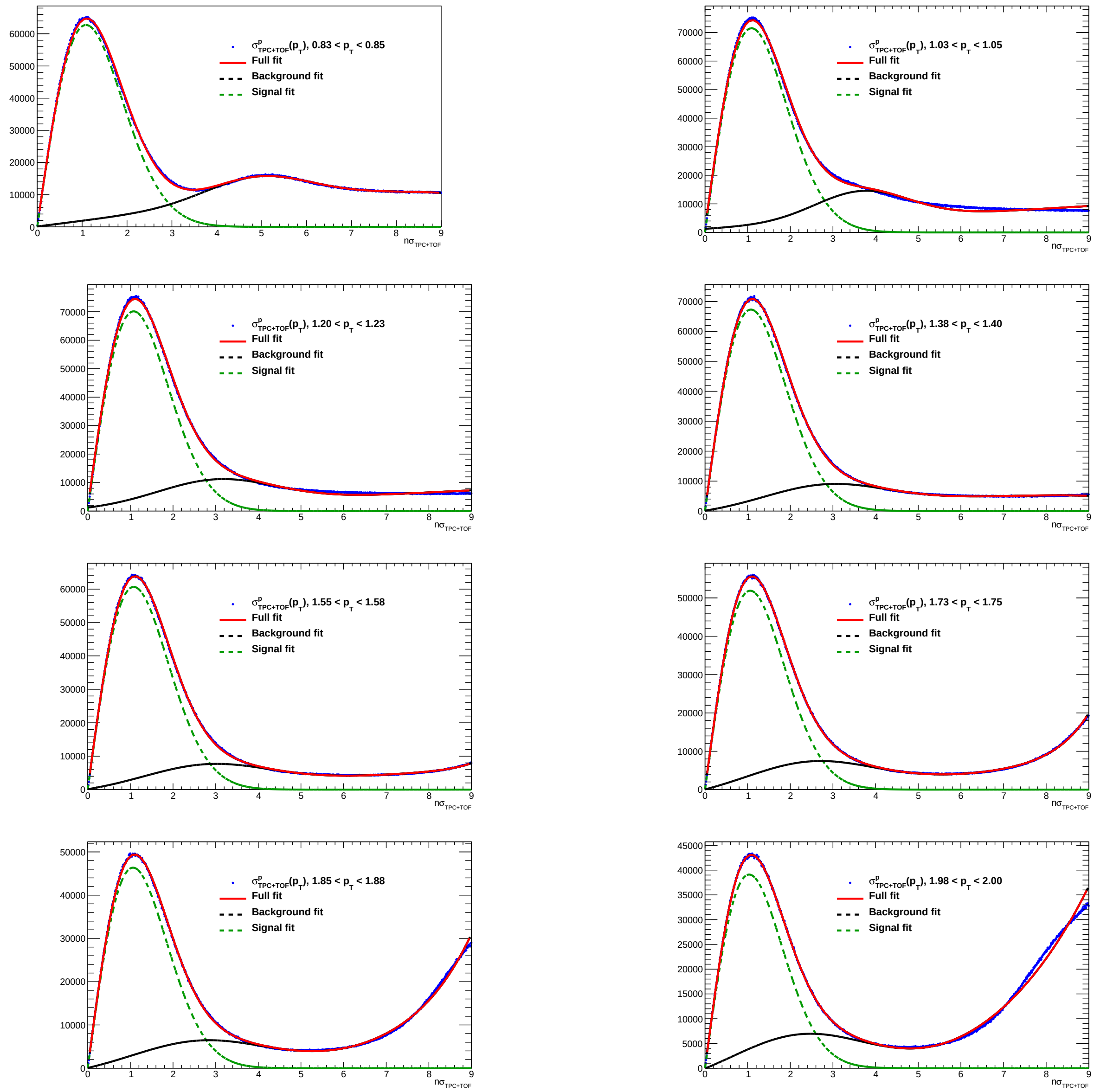

Fig. 17: Some of the particle purity estimation fits of $n\sigma_{comb}$ projections in p_t bins for the zzm_medium dataset. In general, fits were done in p_t intervals the size of 0.02 GeV/c, between 0 and 2 GeV/c, for zzm_medium, zzi and zzo_medium datasets.

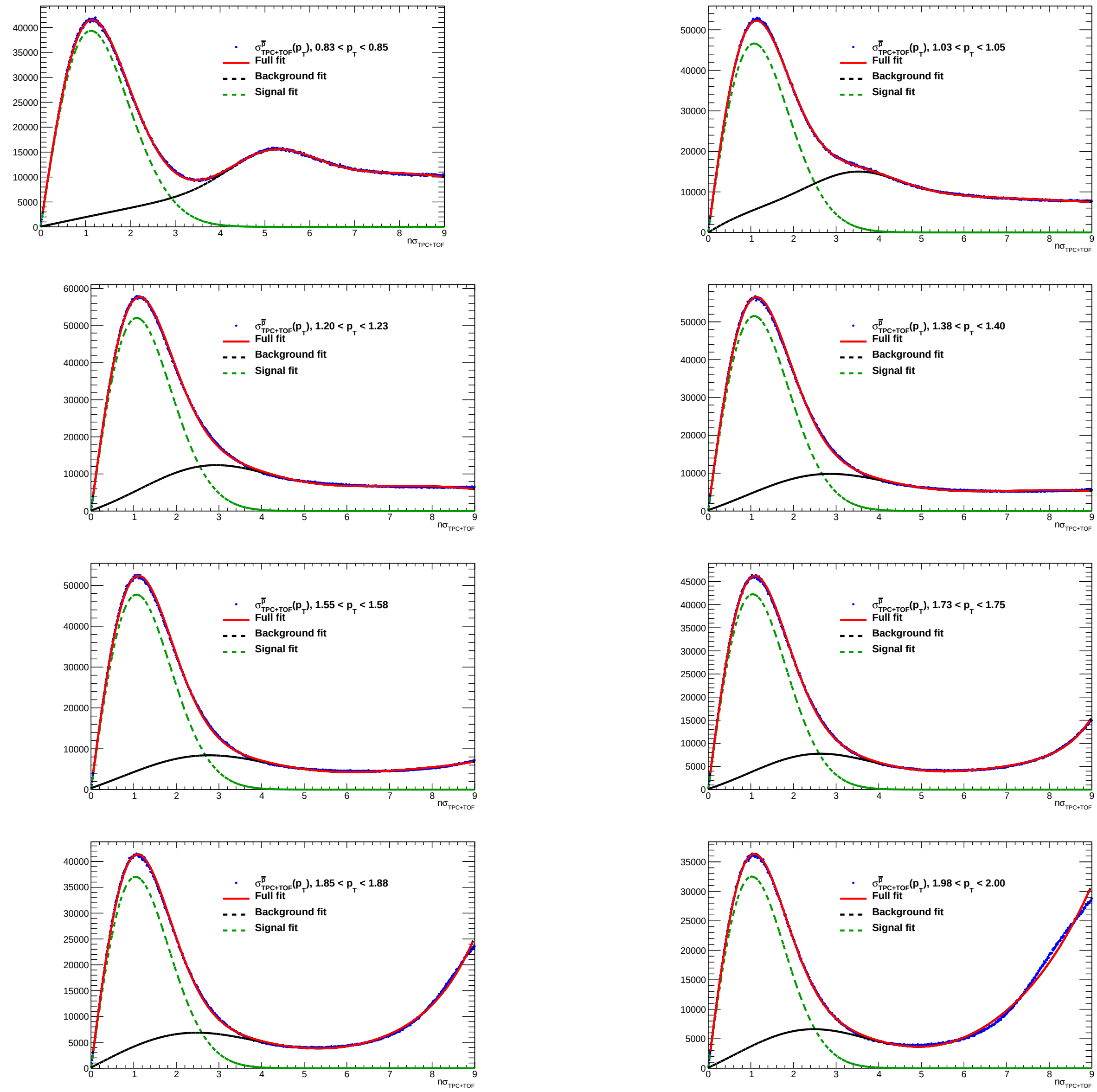

Fig. 18: Some of the antiparticle purity estimation fits of $n\sigma_{comb}$ projections in p_t bins for the zzm_medium dataset. In general, fits were done in p_t intervals the size of 0.02 GeV/c, between 0 and 2 GeV/c, for zzm_medium, zzi and zzo_medium datasets.

Reweighting and normalisation

In order to calculate correlation functions correctly, one must first reweight the mixed event distributions so that they would better represent the same event distributions as a function of multiplicity, see Fig. 19.

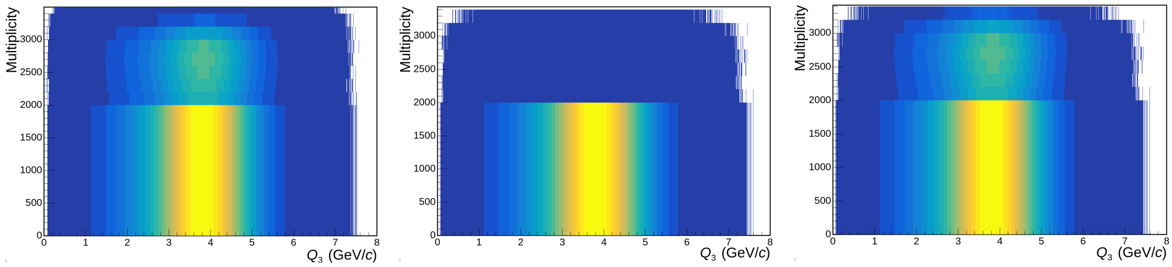

Fig. 19: Same event distribution for the zzm_medium dataset, followed by the mixed event distribution before and after reweighting.

In this analysis, reweighting was done by first taking the Y-axis projection of the ”relTripletQ3Mult” multiplicity vs Q_3 histograms for each centrality bin for the same and mixed events. Next, ratios are obtained by dividing the same-event projections by the mixed-event ones. Then, we loop through the mixed-event Multiplicity vs Q_3 2D histogram, multiplying each bin value by the respective weight (same weight for each bin value in a column), making sure to also reweight the errors.

The same process is done separately for particles and antiparticles in each period. Then, particle distributions from these periods are added up; the same is done for antiparticles. Then, they are combined together. To be able to do so, we need to ensure that the corresponding correlation functions are compatible. Fig. 20 show the particle - antiparticle correlation function comparisons for the zzm dataset (left panel) and the zzi dataset (right). From here we can see that the particle and antiparticle correlation functions are in good agreement at Q_3 range below 2 GeV/c, with Fig. 21 (particle and antiparticle correlation function, obtained using all 8 data-taking periods, comparisons) confirming this.

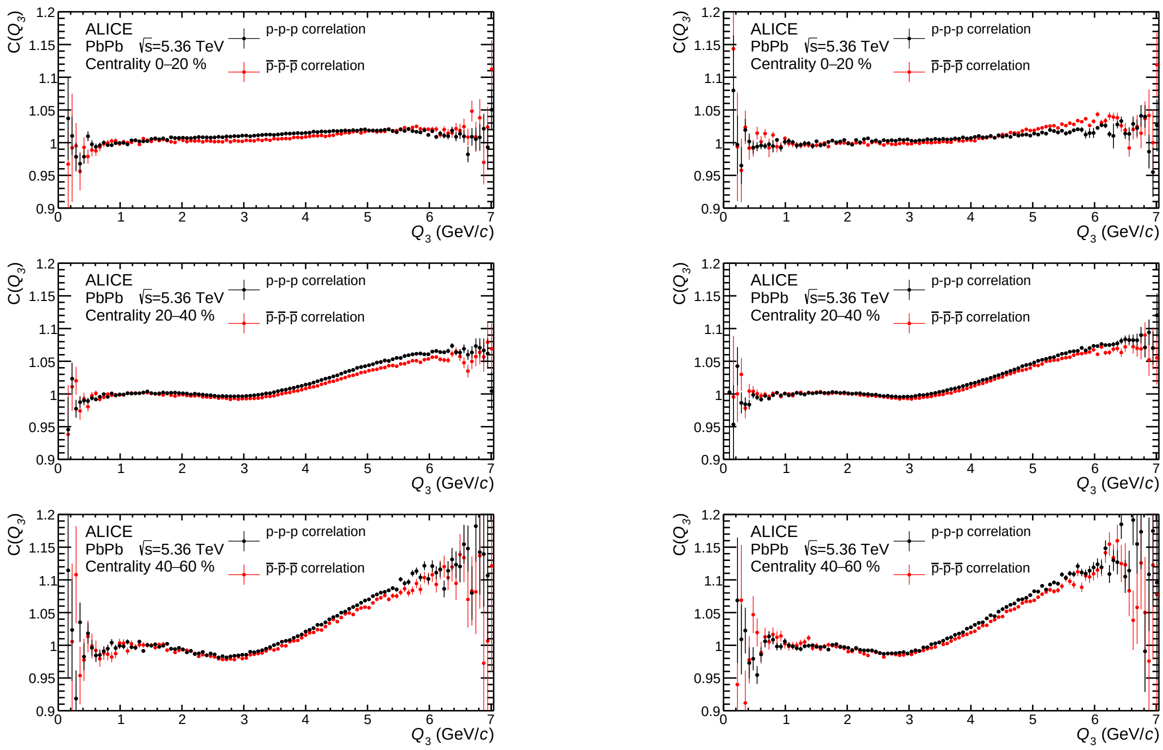

Fig. 20: Particle and antiparticle correlation functions in different centrality ranges, obtained using data from the zzm (left) and zzi (right) datasets, using the selection criteria described in Table 2.

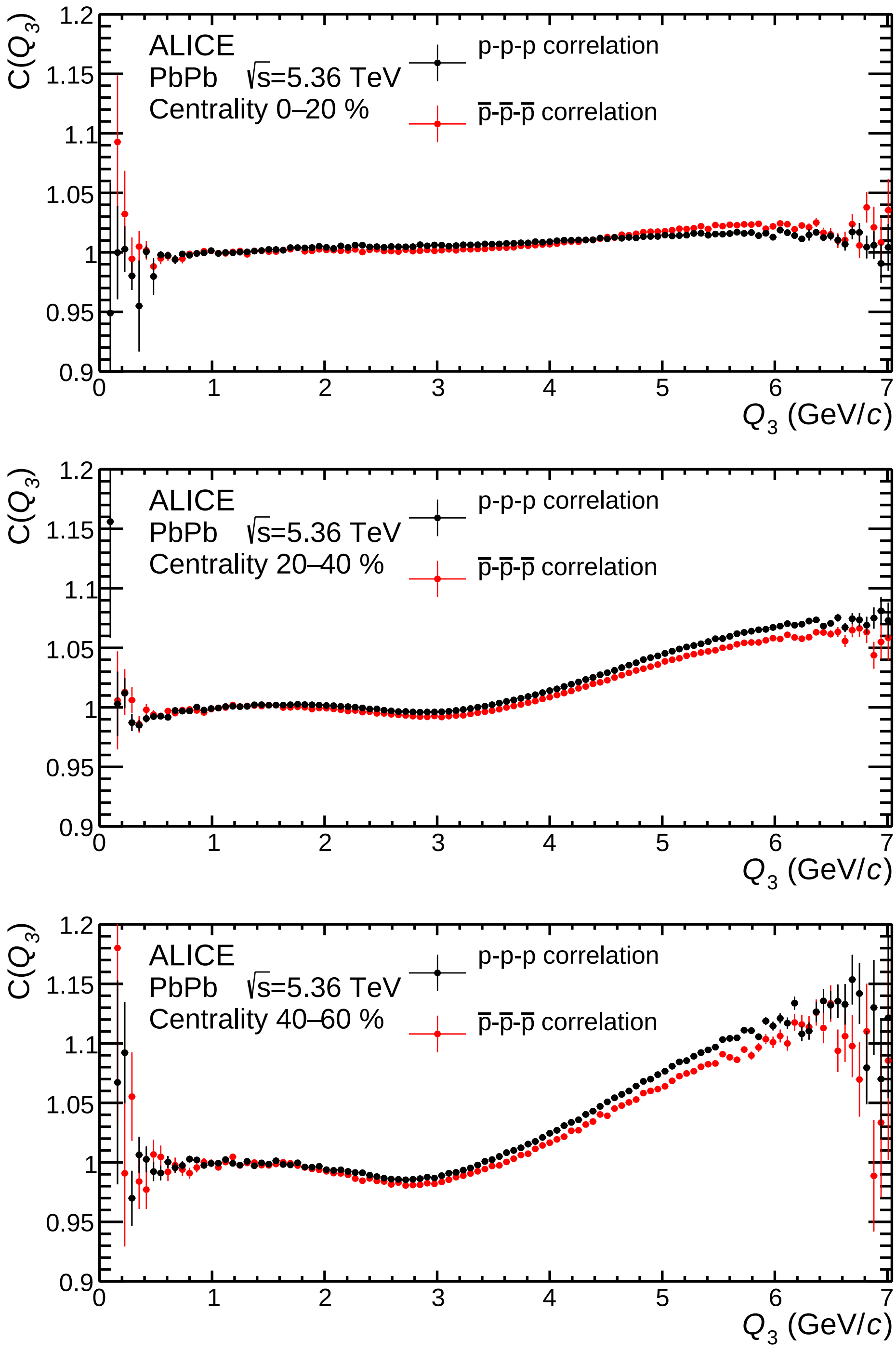

Fig. 21: Particle and antiparticle correlation functions in different centrality ranges, obtained using all 9 data-taking periods, using the selection criteria described in 2

After this, the X-projection of the multiplicity vs Q_3 histograms are taken (both for same and mixed events). The same-event distribution is then divided by the mixed-event one, obtaining the non-normalised correlation function. To obtain the final correlation function, we normalise it so that the function would be equal to unity between Q_3 1 and 1.2 GeV/c (scaling the ratio by the mean in this Q_3 range). The example in difference between non-normalised and normalised correlation function for particles (zzm_medium dataset) can be seen in Fig. 22.

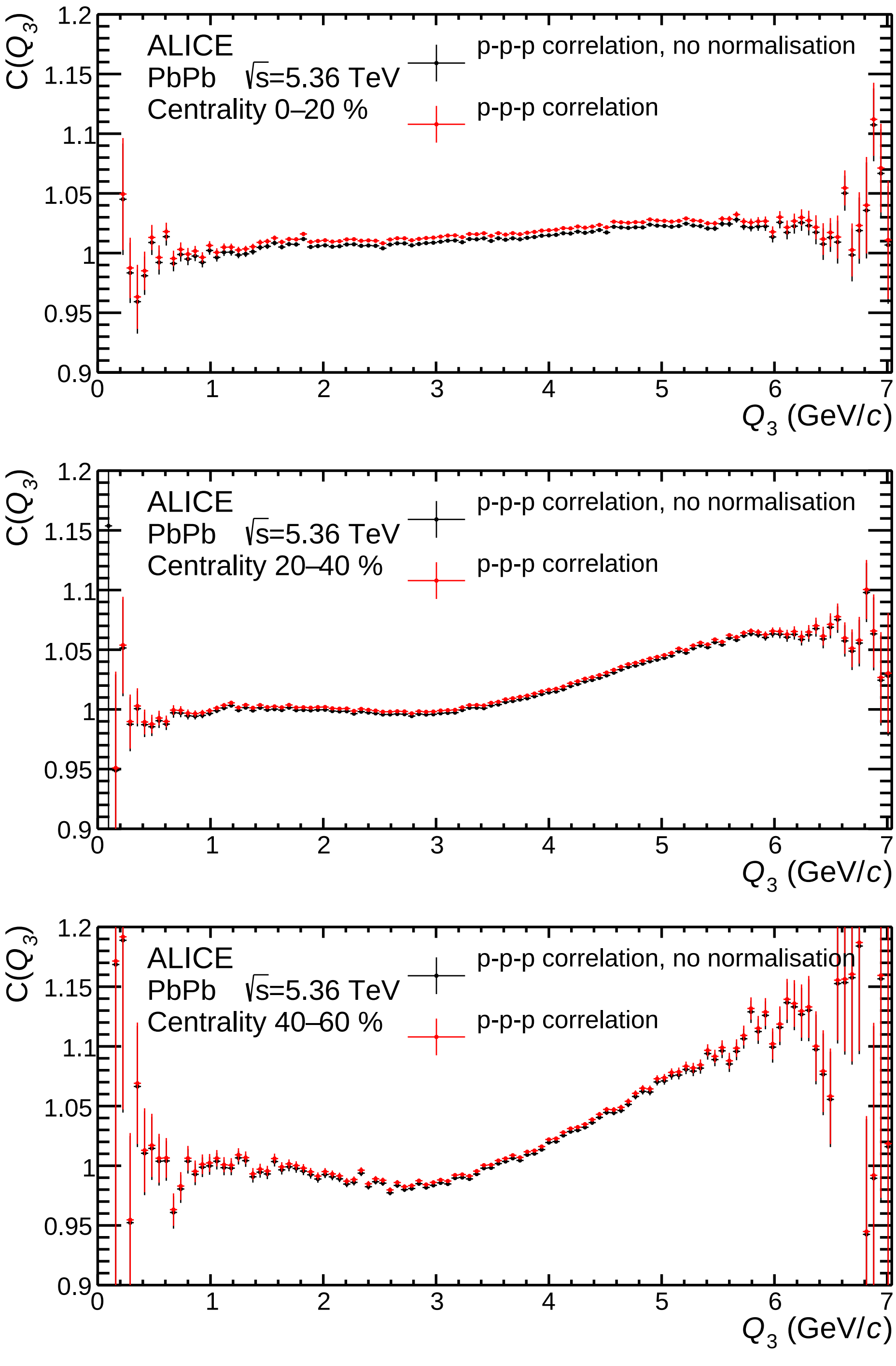

Fig. 22: Particle correlation functions before and after normalisation in different centrality ranges.

Results

To estimate the expected Q_3 range of the signal, the projector method is used. It is done by taking the two-particle correlation function and projecting it onto the 3D phase space. From these projections one can obtain how the correlation function would look like if there were no genuine three body effects taking place [6]. The transformation is described by the integral in the momentum space, seen in Eq. 7. Here W is a projector function which depends only on the masses of the two particles. More information on this can be found in Ref. [5].

$$C_{ji}(Q_3) = \int C(k^*_{ij}) W_{ij}(k^*_{ij}, Q_3) dk^*_{ij} \tag{7}$$

Figures 23 - 24 show the final correlation ($ppp \oplus \bar{p}\bar{p}\bar{p}$) functions obtained in this analysis. The correlation functions obtained in $60\% - 80\%$ and $80\% - 100\%$ centrality percentages are relatively imprecise, so more data would be needed to see the true shape. The correlation functions in the $0\% - 20\%$, $20\% - 40\%$ and $40\% - 60\%$ centrality ranges are in good agreement with the preliminary expected signal ranges (green bands), obtained using the projector method described above. As the projector method requires a two-particle correlation function which includes experimental effects, we use the ones which have been measured by ALICE in the same PbPb Run 3 data sample by Gleb Romanenko (the results have been made available as preliminary figures [1].) The shown ranges are only preliminary as the selection criteria and exact centrality bins are slightly different for the two analysis. Going forward, the two-particle correlation should be obtained also within the framework of the current work.

In the future, our measured correlation functions should be modelled with the full fledged three-body calculations. This will allow theorists to test their predictions.

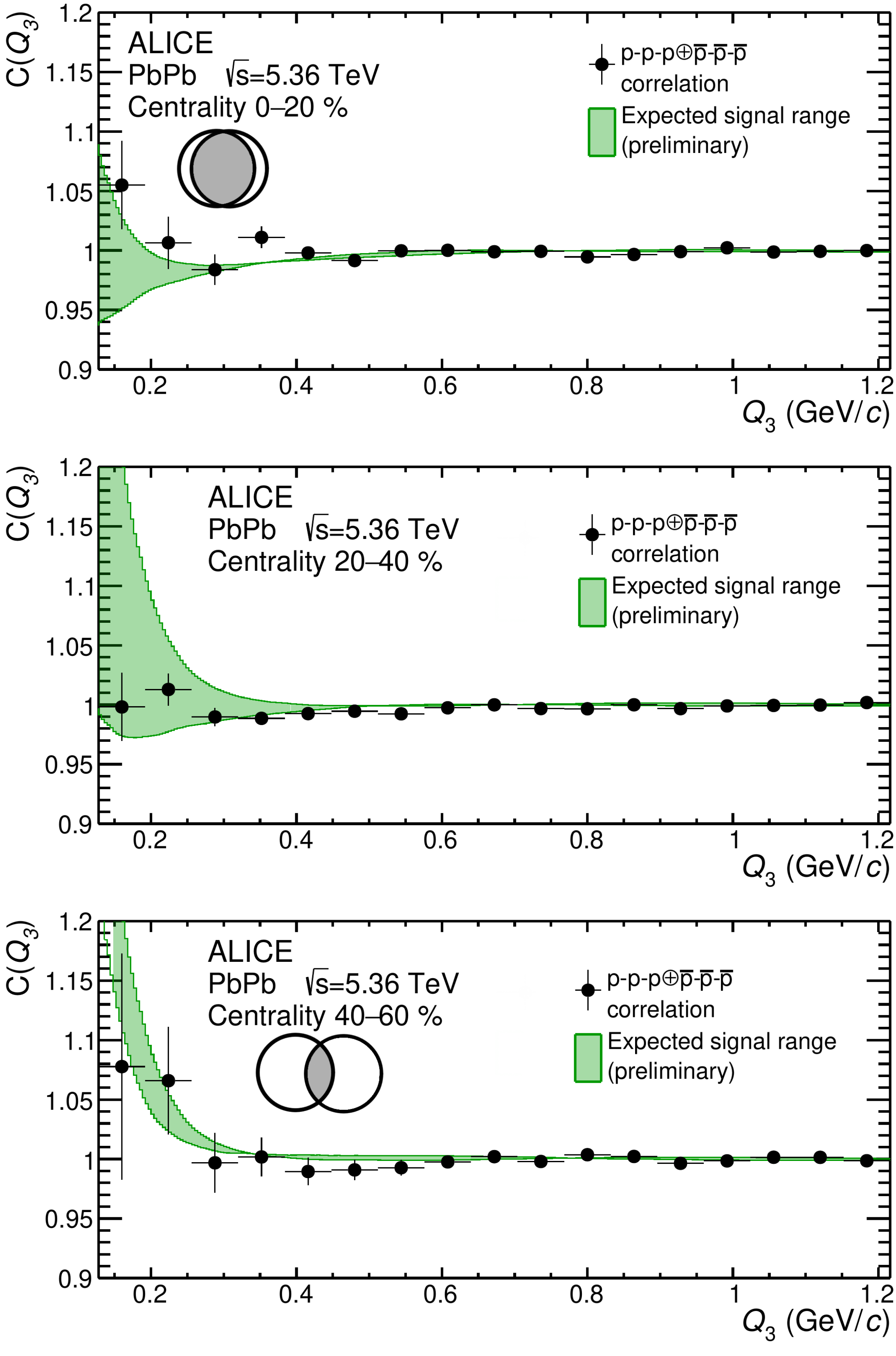

Fig. 23: p-p-$p \oplus \bar{p}$-$\bar{p}$-$\bar{p}$ correlation functions in different centralities (from the 0%-60% centrality range), obtained by adding up data from 8 of the data-taking periods of 2023. Preliminary expected signal range, obtained using the projector method, is included.

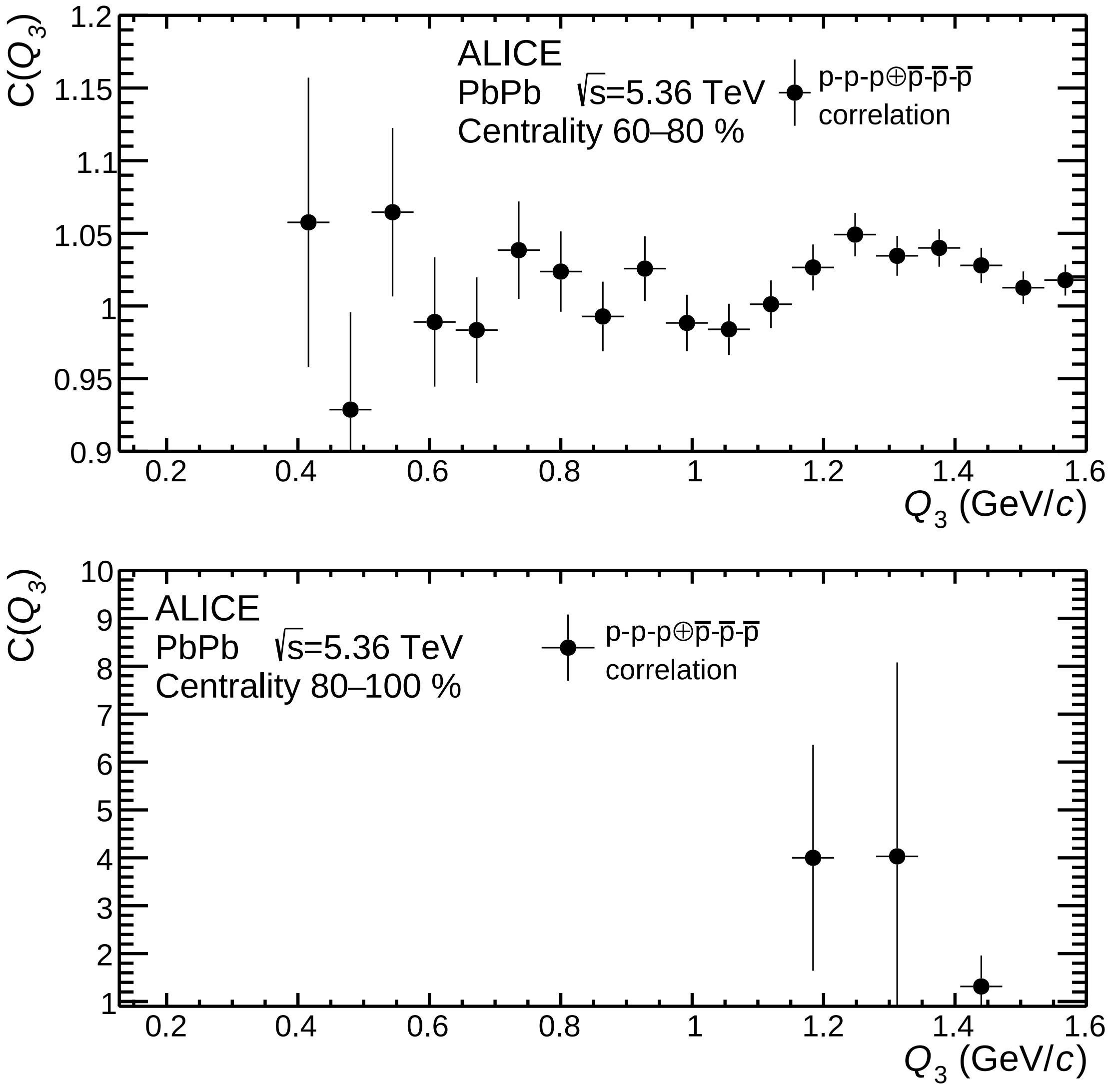

Fig. 24: p-p-$p \oplus \bar{p}$-$\bar{p}$-$\bar{p}$ correlation functions in different centralities (from the 60%-100% centrality range), obtained by adding up data from 8 of the data-taking periods of 2023.

References

[1] Proton pair femtoscopy in Pb–Pb Run3 data. ALICE Internal Note. `https://alice-notes.web.cern.ch/node/1527`.

[2] Three-body correlation functions of ppp and ppΛ systems measured in pp collisions at $\sqrt(s) = 13.6$ TeV. ALICE Internal Note. `https://alice-notes.web.cern.ch/node/1520`.

[3] K. Aamodt et al. The ALICE Experiment at the CERN LHC. *J. Instrum.*, 3:S08002, 2008.

[4] Shreyasi Acharya et al. ALICE upgrades during the LHC Long Shutdown 2. *JINST*, 19(05):P05062, 2024.

[5] ALICE Collaboration. Towards the understanding of the genuine three-body interaction for p–p–p and p–p–λ. *The European Physical Journal A*, 59(7), July 2023.

[6] Raffaele Del Grande, Laura Šerkšnytė, Laura Fabbietti, Valentina Mantovani Sarti, and Dimitar Mihaylov. A method to remove lower order contributions in multi-particle femtoscopic correlation functions. *The European Physical Journal C*, 82(3), March 2022.

[7] E. Garrido, A. Kievsky, R. Del Grande, L. Serksnyte, M. Viviani, and L. E. Marcucci. Convergence of the ppp correlation function within the hyperspherical adiabatic basis, 2025.

[8] A. Kievsky, E. Garrido, M. Viviani, L. E. Marcucci, L. Serksnyte, and R. Del Grande. nnn and ppp correlation functions. *Phys. Rev. C*, 109(3):034006, 2024.

[9] I. Vidana, V. Mantovani Sarti, J. Haidenbauer, D. L. Mihaylov, and L. Fabbietti. Neutron star properties and femtoscopic constraints, 2025.